
National Electrical Manufacturers Association NU-4 Performance Evaluation of the PET Component of the NanoPET/CT Preclinical PET/CT Scanner

Istvan Szanda¹, Jane Mackewn¹, Gergely Patay², Peter Major², Kavitha Sunassee¹, Gregory E. Mullen¹, Gabor Nemeth², York Haemisch³, Philip J. Blower¹, and Paul K. Marsden¹

¹Division of Imaging Sciences and Biomedical Engineering, King's College London, London, United Kingdom; ²Mediso Ltd., Budapest, Hungary; and ³Bioscan Inc., Washington, District of Columbia

The NanoPET/CT represents the latest generation of commercial preclinical PET/CT systems. This article presents a performance evaluation of the PET component of the system according to the National Electrical Manufacturers Association (NEMA) NU-4 2008 standard. **Methods:** The NanoPET/CT consists of 12 lutetium yttrium orthosilicate:cerium modular detectors forming 1 ring, with 9.5-cm axial coverage and a 16-cm animal port. Each detector crystal is $1.12 \times 1.12 \times 13$ mm, and 1 module contains 81×39 of these crystals. An optical light guide transmits the scintillation light to the flat-panel multianode position-sensitive photomultiplier tubes. Analog-to-digital converter cards and a field-programmable gate array-based data-collecting card provide the readout. Spatial resolution, sensitivity, counting rate capabilities, and image quality were evaluated in accordance with the NEMA NU-4 standard. Energy and temporal resolution measurements and a mouse imaging study were performed in addition to the standard. **Results:** Energy resolution was 19% at 511 keV. The spatial resolution, measured as full width at half maximum on single-slice rebinning/filtered backprojection-reconstructed images, approached 1 mm on the axis and remained below 2.5 mm in the central 5-cm transaxial region both in the axial center and at one-quarter field of view. The maximum absolute sensitivity for a point source at the center of the field of view was 7.7%. The maximum noise equivalent counting rates were 430 kcps at 36 MBq and 130 kcps at 27 MBq for the mouse- and rat-sized phantoms, respectively. The uniformity and recovery coefficients were measured with the image-quality phantom, giving good-quality images. In a mouse study with an ¹⁸F-labeled thyroid-specific tracer, the 2 lobes of the thyroid were clearly distinguishable, despite the small size of this organ. The flexible readout system allowed experiments to be performed in an efficient manner, and the system remained stable throughout. **Conclusion:** The large number of detector crystals, arranged with a fine pitch, results in excellent spatial resolution, which is the best reported for currently available commercial systems. The absolute sensitivity is high over the field of view. Combined with the excellent image quality, these features make the NanoPET/CT a powerful tool for preclinical research.

Key Words: NanoPET; small-animal PET scanner; performance evaluation; instrumentation; molecular imaging

J Nucl Med 2011; 52:1741-1747

DOI: 10.2967/jnumed.111.088260

The NanoPET/CT (Bioscan Inc., manufactured by Mediso Ltd.) represents the latest generation of commercial small-animal PET/CT systems incorporating state-of-the-art materials and techniques. The major aim of the development was to provide a high-resolution, high-sensitivity PET/CT device for preclinical research in a compact design meeting industrial quality standards. This article evaluates the performance parameters of the NanoPET/CT scanner, based on the National Electrical Manufacturers Association (NEMA) NU-4 2008 standard (1). The standard involves measurements of the spatial resolution; scatter fraction, count losses, and random coincidence rate; sensitivity; and image quality, accuracy of attenuation, and scatter corrections. Three additional measurements were also performed: temporal and energy resolution and an example imaging study.

MATERIALS AND METHODS

Scanner Description

The NanoPET/CT system was designed to be compact and allow sequential PET and CT in a single session for small animals with good access to the animal and a minimum axial coverage of 9.5 cm. Figure 1A shows a photo of the PET ring. The key geometric parameters of the PET component of the scanner, in comparison with other small-animal PET scanners, are given in Table 1. Each of the 12 detector modules comprises an array of 39×81 lutetium yttrium orthosilicate:cerium (LYSO:Ce) crystals on a pitch of 1.17 mm, read out by 2 multianode position-sensitive photomultipliers (H9500; Hamamatsu). An optimized thin light guide (2) permits identification of all crystals in the array as can be seen in Figure 1B. More information about the ring itself and mechanical parameters can be found in an article by Major et al. (2). Groups of 3 modules are connected to 4 analog-to-digital converter cards. A field-programmable gate array processes the data in real time and sends them to the PET acquisition computer in

Received Mar. 25, 2011; revision accepted Jul. 19, 2011.

For correspondence or reprints contact: Istvan Szanda, King's College London, Division of Imaging Sciences and Biomedical Engineering, 4th Floor Lambeth Wing, St. Thomas Hospital, London SE1 7JY, U.K.

E-mail: istvan.szanda@kcl.ac.uk

Published online Oct. 3, 2011.

COPYRIGHT © 2011 by the Society of Nuclear Medicine, Inc.

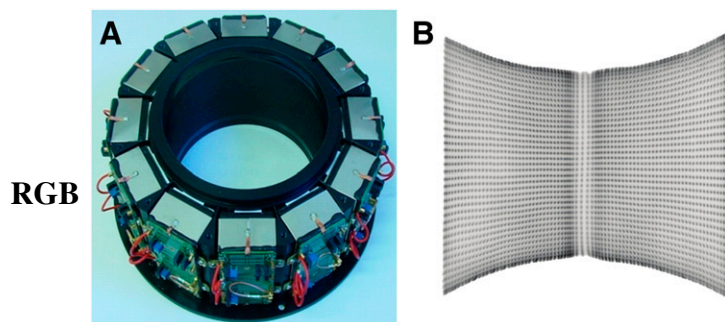


FIGURE 1. (A) PET ring with 12 modules. Each module contains 2 photomultiplier tubes, but they are connected to same circuit board. (B) Flood-field image of PET module. Because of optimized light guide, spots of 81×39 crystal needles are clear and distinguishable, even in gap between 2 tubes.

which they are stored in list-mode format. All readout electronics and acquisition computers are housed within the compact scanner gantry. Energy and position calibrations based on look-up tables are applied to differentiate the large number of crystal elements—both their location within an array and the position of their photopeak (2). The numbers of modules in coincidence (just the opposing one [1–1] or its ± 1 [1–3] or ± 2 [1–5] neighbors) can be defined to optimize the trade-offs between spatial resolution, sensitivity, and field of view (FOV) for different applications. Readout is extremely flexible—the events in every acquisition are stored in list-mode format with their energy, position coordinate, and time stamp

information. Several options to refilter the data are provided. For instance, different time coincidence or energy windows can be applied, and data can be divided into dynamic time frames. All these operations can be performed retrospectively on the list-mode data. Normalization was based on the Defrise method (3). Currently, list-mode data are binned using single-slice rebinning (SSRB) (4) into 2-dimensional (2D) line-of-response data files or into a set of 2D sinograms for reconstruction using filtered-backprojection (FBP) (5), ordered-subset expectation maximization (OSEM) (6), or maximum-likelihood expectation maximization (7). A fully 3-dimensional (3D) reconstruction algorithm, taking advantage of the high intrinsic resolution of the scanner, has recently been made available but was not used in the current evaluation.

Energy and Temporal Resolution

A NEMA ^{22}Na point source (MMS-09 022-25U type; Eckert-Ziegler Isotope Products GmbH) was used in this measurement. It has a 0.25-mm active spot size embedded in a 1-cm³ acrylic cube. Its activity, measured in a calibrated dose calibrator (CRC-15r; Capintec, Inc.), was 1.014 MBq. The point source was positioned in the center of the field of view (CFOV) axially and transaxially. Data were acquired for 60 s in 1–5 coincidence mode, with a coincidence window of 5 ns and energy window of 250–750 keV. From the list-mode data, all events were sorted into 1-keV-wide histogram bins for energy resolution assessment and 156.25-ps (equal to the unit of the time-stamp)-wide histogram bins for temporal resolution. Full width at half maximum (FWHM) values were determined.

TABLE 1
Comparison of Design of Selected Small-Animal PET Systems

Category	Quad-HIDAC (14,15)	microPET II (11)	VISTA (16)	Inveon (10)	NanoPET/CT
Detector					
Crystal material	Avalanche chamber detector	Lutetium oxyorthosilicate	LYSO:Ce and GSO dual-layer	LSO	LYSO:Ce
Crystal size (mm)	0.4-hole size	$0.975 \times 0.975 \times 12.5$	$1.45 \times 1.45 \times 7$ LYSO:Ce; $1.45 \times 1.45 \times 8$ GSO	$1.51 \times 1.51 \times 10$	$1.12 \times 1.12 \times 13$
Crystal pitch (mm)	0.5-hole pitch	1.15	1.55	1.59	1.17
Packing fraction	80%	72%	88%	90%	92%
Crystal array	311×188 holes	$196 (14 \times 14)$	$169 (13 \times 13)$	$400 (20 \times 20)$	$3,159 (81 \times 39)$
System					
No. of detector blocks/module	4	90	36	64	12
No. of crystals	233,872 holes	17,640	$6,084 \times 2$	25,600	37,908
No. of rings	311	42	26	80	81
No. of crystals per ring	752	420	234	320	468
Ring diameter (cm)	17	16	11.8	16.1	18.1
Gantry aperture (cm)	17	15.3	8	12	16.0
Axial FOV (cm)	28	4.9	4.8	12.7	9.48
Transaxial FOV (cm)	17	8	6.7	10.0	12.3
Solid angle/ 4π	0.75	0.16	0.23	0.62	0.32
Dataset					
No. of sinograms					
3D	NA	1764	NA	6,400	6,561
2D	NA	83	61	159	161
Sinogram size	NA	140×210	128×175	128×160	410×240
Sampling distance (mm)	0.1–1	0.575	NA	0.815	0.3

NA = not applicable.

Spatial Resolution

The source used for the spatial resolution measurement was the same NEMA ^{22}Na point source as described in the “Energy and Temporal Resolution” section. Following the NEMA protocol, the spatial resolution values were not corrected for the size of the source, photon range, or noncollinearity. The source was positioned into 2 axial positions (CFOV and one-quarter FOV) and 6 radial positions (0, 5, 10, 15, 25, and 35 mm from the axis of the scanner per axial position). The list-mode data were acquired in 1–5 coincidence mode, with an energy window of 250–750 keV and coincidence window of 5 ns. Data were normalized to correct for different detection efficiencies and then rebinned into a set of 0.3-mm bin-sized 2D sinograms using the SSRB method with a ring difference of 8 and 81. The reconstruction method was 2D FBP, with a Ram-lak filter (1.0 cutoff frequency), resulting in a reconstructed image with 0.585-mm axial plane thickness and 0.15-mm pixel size. One-dimensional response functions were drawn in each dimension, and their FWHM and full width at tenth maximum values were measured.

Sensitivity

The source specified in the “Spatial Resolution” section was used to determine the sensitivity of the PET scanner. It was positioned in the center of the scanner, both axially and transaxially, and then stepped in 0.585-mm increments in the axial direction to both ends of the scanner, performing a 55-s scan at each position. List-mode data were acquired in 1–5 coincidence mode, with an energy window of 250–750 keV and coincidence window of 5 ns, and rebinned into a set of 0.3-mm bin-sized 2D sinograms using the SSRB method without scatter correction. Because the intrinsic radiation of the LYSO:Ce crystals (8) can cause true coincidences, the background counting rate was collected with the same acquisition parameters and subtracted from each sinogram. To obtain the absolute sensitivity at each source position, the total number of counts over all the masked slices was summed and divided by the activity and the branching ratio of the point source in accordance with the NEMA specification (^{22}Na , 0.9060). Twelve percent sensitivity loss due to photon attenuation was estimated, assuming the water equivalency of the plastic cube, and a correction for this sensitivity was applied. In addition to the absolute sensitivity for each source position, average absolute sensitivities were calculated for a mouse-length region (7 cm) and a rat-length region (whole axial FOV) by averaging the absolute sensitivities for all source positions within the relevant region.

Scatter Fraction, Counting Rate Losses, and Random Coincidence Rate Measurements

In accordance with the NEMA protocol, scatter fraction and counting rate performance were measured with 2 different high-density polyethylene (0.96 g/cm^3) phantoms centered in the scanner both axially and transaxially. A mouselike phantom (70-mm length, 25-mm diameter) (part no. 60-00-40; Mediso Ltd.) with a 2.5-mm-inner-diameter line source positioned 10 mm off-center along the axis of the phantom was filled with 80 MBq of ^{18}F measured in a calibrated dose calibrator (CRC-15r; Capintec, Inc.). A ratlike phantom (150-mm length, 50-mm diameter) (part no. PH-60-00-41; Mediso Ltd.) with a 2.5-mm-inner-diameter line source positioned 17.5 mm off-center along the axis of the phantom was similarly filled with 60 MBq of ^{18}F . Dynamic scans were obtained in 1–5 coincidence mode, with 250- to 750-keV energy

and 5-ns coincidence windows, until the activity of the line source decayed to below 23.5 kBq. With the same settings, an empty phantom was scanned for 54,000 s to calculate the background due to the intrinsic radiation of ^{176}Lu in the LYSO:Ce crystals (8). Every dataset was sorted into sets of 2D sinograms using the SSRB method (0.3-mm bin size and 0.585 slice thickness) with 250- to 750-keV energy and 5-ns coincidence window. Calculations of the total and true event rates were performed in accordance with the NEMA standard. The scatter fraction was calculated by Equation 1 at activities between 1 and 1.5 MBq, for which the random event rate is negligible compared with the scatter event rate. Using this scatter fraction and assuming that it is constant at every activity level, we calculated the random rate by a method described in the NEMA standard.

$$SF = \frac{R_s}{R_t + R_s}, \quad \text{Eq. 1}$$

where SF is the scatter fraction, R_s is the scattered event rate, and R_t is the true event rate.

The noise-equivalent counting (NEC) rate of each acquisition is calculated by Equation 2:

$$\text{NEC} = \frac{R_t^2}{R_{\text{TOT}} + R_r}, \quad \text{Eq. 2}$$

R_{TOT} is the total event rate, and R_r is the random event rate.

NEMA Image-Quality Phantom Study

The NU-4 mouse image-quality phantom (part no. PH-60-00-42; Mediso Ltd.), made of polymethylmethacrylate, has 3 main parts (Fig. 2). The first is a homogeneous block filled with radioactivity (30-mm diameter and 30-mm length) to measure the signal-to-noise ratio of the system. The second part consists of 2 chambers filled with cold water and air (length, 15 mm; outer diameter, 10 mm; wall thickness, 1 mm) to estimate the scatter fraction in the image. The third part is a plastic region (30-mm diameter, 20-mm length) with 5 rods drilled through with various diameters (1, 2, 3, 4, and 5 mm)

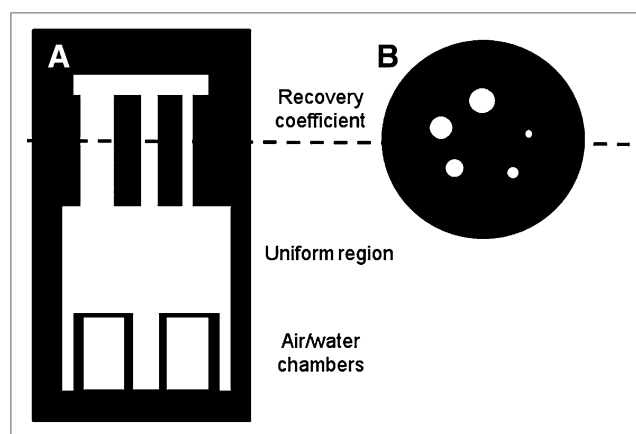


FIGURE 2. NEMA NU-4 image-quality phantom contains the following 3 regions: region with 5 rods (diameter, 1, 2, 3, 4, and 5 mm) to measure recovery coefficients (A; top), homogeneous region to measure uniformity (A; middle), and 2-chamber region (air- and water-filled) to measure background in reconstructed image (A; bottom). (B) Five-rod region.

to measure the recovery coefficient curve. The phantom was filled with 3.7 MBq of ¹⁸F, and the duration of the scan was 20 min. The following data acquisition parameters were used: 5-ns coincidence window and 250- to 750-keV energy window in 1–5 coincidence mode. Crystal efficiency correction was applied. The list-mode data were rebinned using 2D line-of-response SSRB with an 81-ring difference; the reconstruction process was maximum-likelihood expectation maximization with 50 iterations, a pixel size of 0.3 mm, and a slice thickness of 0.585 mm.

Uniformity was measured by drawing a 22.5-mm-diameter by 10-mm-long cylindrical volume of interest over the center of the phantom. Average pixel value and coefficient of variation were determined. To measure the recovery coefficients, the 10-mm central portion of the length of the rods was averaged to reduce the noise. Cylindric regions of interest with diameters twice the physical diameters of the rods were drawn around the rods. Linear profiles were drawn along the rods in the axial direction. Assuming that the recovery coefficient of the homogeneous region is equal to 1, the average pixel values of the linear profiles were divided by the average pixel value of the uniform region to determine the recovery coefficients. The SD of the recovery coefficients were calculated by Equation 3.

$$SD_{RC} = \sqrt{\left(\frac{SD_{line\ profile}}{Mean_{line\ profile}}\right)^2 + \left(\frac{SD_{uniform\ region}}{Mean_{uniform\ region}}\right)^2}, \quad \text{Eq. 3}$$

The scatter fraction in the image was measured by defining volumes of interest in the cold regions (4-mm diameter and 7.5-mm length) and dividing the average pixel values in these regions by the average pixel value in the uniform region.

Animal Study

A 10-wk-old BALB/C female mouse was scanned after administration of 5 MBq of a PET thyroid imaging agent, ¹⁸F-tetrafluoroborate (9). Thirty minutes after tail vein injection of the tracer, the mouse was imaged for 30 min. The following data acquisition parameters were used: 5-ns coincidence window and 250- to 750-keV energy window in 1–5 coincidence mode. Crystal efficiency correction was applied. The rebinning method was SSRB, with a ring difference of 8, and the reconstruction process was OSEM (subsets, 6; iterations, 8). Pixel size was 0.3 mm, and the slice thickness was 0.585 mm. A summary of the measurement parameters is presented in Table 2.

RESULTS

Energy and Temporal Resolution

The energy resolution of the 511-keV photopeak was 19% based on the average of every detector in the scanner. The value of the temporal resolution depends on the coincidence mode and the energy window, varying from 1.55 ± 0.2 ns (1:1 coincidence mode, 400- to 600-keV energy window) to 3.25 ± 0.72 ns (1:5 coincidence mode, 250- to 750-keV energy window). This variation is likely to be due to the relatively large effect of intercrystal scatter in a scanner with small crystal dimensions, and the optimum value for the timing window will depend on the imaging situation.

TABLE 2
Summary of Measurement Parameters

Measurement	Source	Activity (MBq)	Energy window	Coincidence mode	Coincidence window	Location of source	Rebinning, reconstruction voxel size/slice thickness
Spatial resolution	²² Na (0.25 mm) ³	1.014	250–750 keV	1–5	5 ns	See text	SSRB/FBP, 0.15 mm/0.585 mm; span, 8 and 81
Sensitivity	²² Na (0.25 mm) ³	1.014	250–750 keV	1–5	5 ns	Center of FOV	SSRB, 0.3 mm/0.585 mm; span, 81
Counting rate	NEMA standard mouse/rat phantom	80 (mouse); 60 (rat)	250–750 keV	1–5	5 ns	Phantom in the center of FOV	SSRB, 0.3/0.585 mm; span, 81
Image quality	NEMA standard phantom	3.7	250–750 keV	1–5	5 ns	Phantom in the center of FOV	SSRB/MLEM, 0.15 mm/0.585 mm; span, 81
Energy resolution	²² Na (0.25 mm) ³	1.014	250–750 keV	1–5	5 ns	Center of FOV	Binned into 1-keV/156.25-ps-wide histograms
Temporal resolution	²² Na (0.25 mm) ³	1.014	250–750 keV	1–5	5 ns	Center of FOV	Binned into 1-keV/156.25-ps-wide histograms
Mouse study	¹⁸ F-tetrafluoroborate	5 MBq; 50 μL into tail vein; postinjection timing 30 min	250–750 keV	1–5	5 ns	Whole body in the FOV, 30-min scanning timing	SSRB/OSEM, 0.3 mm/0.585 mm; span, 8

MLEM = maximum-likelihood expectation maximization.

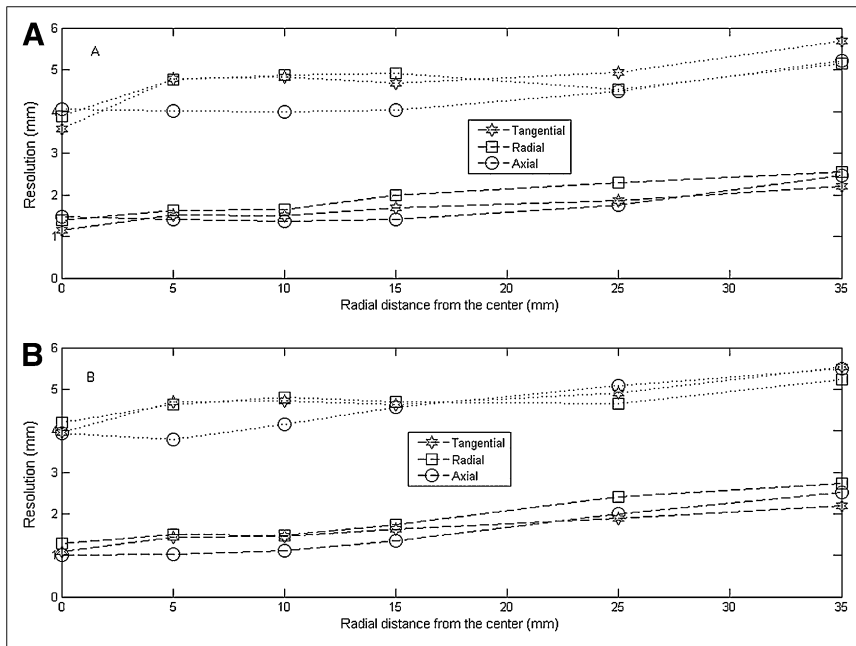


FIGURE 3. Spatial resolution in center of axial FOV (A) and at one-quarter FOV from center (B). Dashed line and dotted line correspond to FWHM and full width at tenth maximum, respectively. On axis, FWHM approached 1 mm and remained below 2.5 mm in central 5-cm region.

Spatial Resolution

Figure 3 shows the FWHM and full width at tenth maximum for the radial, tangential, and axial components of the SSRB FBP reconstructed images. On the axis, the scanner resolution approached 1 mm. Over the central 5-cm transaxial region, the scanner resolution remained under 2.5 mm. If the span was set to 81, the axial resolution in the center was degraded from 1.1 to 2.2 mm because of the use of the SSRB algorithm (the radial and tangential resolutions did not change).

Sensitivity

For the source at the CFOV, the absolute sensitivity was 7.7%. Assuming 12% attenuation, the maximum absolute sensitivity was 8.6%. The average absolute sensitivities for the mouse- and the rat-sized regions were 5.14% and 4.21%, respectively.

Scatter Fraction, Counting Rate Losses, and Random Coincidence Rate Measurements

With an energy window of 250–750 keV and coincidence window of 5 ns in 1–5 coincidence mode, the peaks of the NEC curves were 430 kcps at 36 MBq and 130 kcps at 27 MBq for the mouse and rat phantoms, respectively. The scatter fractions of the 2 phantoms were 15% and 30%, respectively. Figure 4 shows the NEC rate curves as a function of activity for both phantoms.

NEMA Image-Quality Phantom Study

Results from the NEMA image-quality phantom in Figure 5 show the average of the transverse planes in the uniform region (Fig. 5A), the 5-rod region (Fig. 5B), and the 2-chamber region (Fig. 5C). The uniformity of the uniform region was 8%. The scatter fractions in the image of the air- and water-filled chambers were 0.20 ± 0.04 and 0.08 ± 0.02 , respectively. The recovery curve can be seen in Figure 6.

Mouse Study

During the mouse study, the animal-handling facilities provided good accessibility. Figures 7A and 7B, respectively, show coronal and sagittal slices of the SSRB OSEM reconstructed image of the mouse. Both the salivary glands and the lobes of the thyroid are separated in the images, although the size of these structures is small (diameter, ~1 mm; length, ~2 mm). In Figure 7, the right and left arrows show the thyroid and salivary glands, respectively.

DISCUSSION

The scanner behaved in a stable fashion throughout all experiments, which were facilitated by the highly flexible data acquisition and readout.

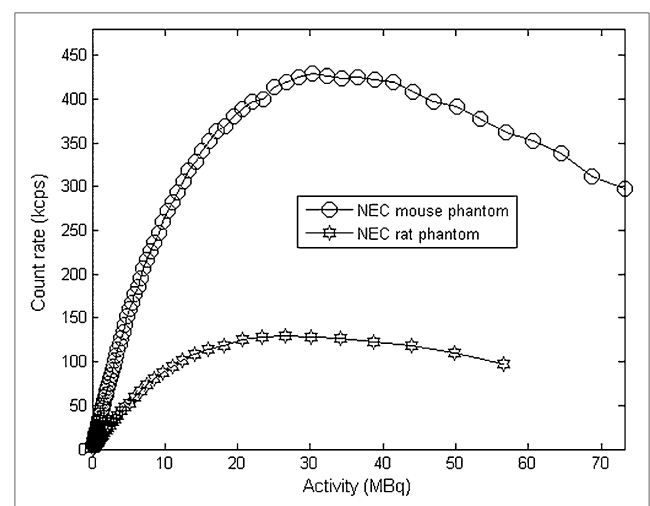


FIGURE 4. NEC rate curves for mouse and rat phantoms as function of activity. Injected activity in our laboratory is typically 2–10 MBq, which is well below NEC peaks.

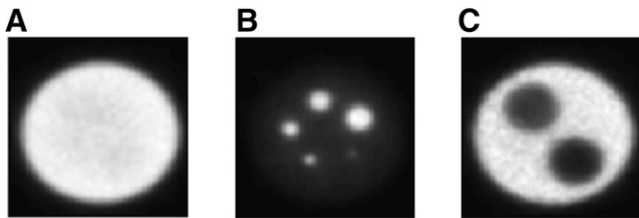


FIGURE 5. Image of NEMA image-quality phantom: uniform region (A), 5-rod region (B), and 2-chamber region (C). Activity distribution in uniform region looks quite homogeneous; all 5 rods are visible. Although scatter correction was not applied, cold air and water regions are distinguishable.

The energy resolution and temporal resolution are comparable to those of other preclinical PET systems with a similar overall configuration, for example, the Inveon (Siemens) (10).

The spatial resolution approaches 1 mm on the axis, making it possible to resolve small structures such as the lobes of the mouse thyroid, and remains below 2.5 mm over the central 5-cm region transaxially, providing a sufficient FOV for rodent imaging. Of the conventional systems, this spatial resolution is surpassed only by the microPET II (11), and examination of the crystal dimensions and scanner geometries in Tables 2 and 3 suggests that the high resolution can be primarily attributed to the fine crystal pitch (2).

The sensitivities of the Quad HIDAC (noncommercial), microPET II, and Vista (GE Healthcare; now Sedecal Argus PET/CT) systems are all much lower than for the Inveon and NanoPET/CT. The slightly higher sensitivity of the Inveon is attributed to its smaller ring diameter (16.1 vs. 18.1 cm) and larger axial extent (12.7 vs. 9.48 cm) (10) than those of the NanoPET/CT. The larger maximum acceptance angle of the Inveon, however, can also lead to reduced axial resolution, and in practice smaller acceptance angles may be used, with an accompanying reduction in sensitivity. The sensitivity of the Inveon is 4.51% using a 350- to 650-keV energy window, 4-ns coincidence window, and span of 46 (in which case, the axial solid angle incorporated by the SSRB algorithm is 0.102) (12). In the case of the NanoPET/CT, the sensitivity is 4.67%—that is, essentially the same as that for the Inveon system—using the same energy and coincidence windows and a span of 70 (resulting in the same solid angle of 0.101).

The axial FOV of the NanoPET/CT is sufficiently large to scan the body of a mouse in 1 bed position. The peak NEC rate of the NanoPET is lower than that of, for example, the Inveon system (10); however, it has been found suitable for

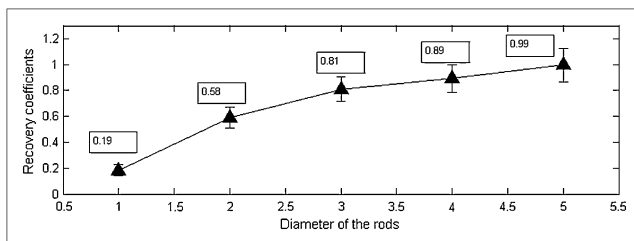


FIGURE 6. Recovery coefficients of rods as function of rod diameter.

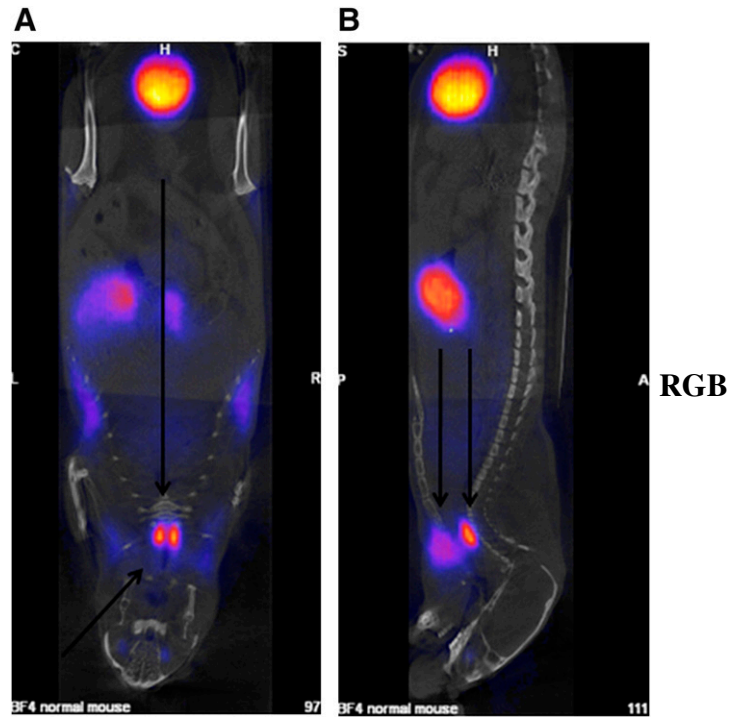


FIGURE 7. Coronal (A) and sagittal (B) slices of SSRB OSEM reconstructed image of mouse injected with 5 MBq of ^{18}F -tetrafluoroborate. Right and left arrows show thyroid and salivary glands, respectively. Two lobes of thyroid are clearly separated.

all experiments conducted in our department, in which injected activities typically range from 1 to 10 MBq. The capability of the NanoPET scanner to image at low activities (1–3 MBq) has been exploited many times. This capability is of particular significance in the development of new tracers for PET, which may be produced in small quantities because of inefficient experimental labeling methods with low specific activities and which are further limited by the small injectable volume (50–200 μL in the case of mice). Imaging at low activities has been found a much bigger challenge than imaging at high activities. In 1985, Muehllehner (13) demonstrated that fewer counts at higher spatial resolution provide an image quality equal to that obtained with many more counts but at lower spatial resolution. The excellent spatial resolution offered by the system may therefore lead to good image quality with smaller injected activities and counting rates than might be expected with lower-resolution systems.

The image uniformity measurement is influenced by the lack of attenuation correction (not implemented at the time of the measurement), which is responsible for the clear reduction in intensity at the center of the cylinder. The pixel values at the center of the cylinder are approximately 11% lower than at the edge. Application of an attenuation-correction procedure would address this in a straightforward way. In the case of the water- and air-filled regions, the scatter fractions may be significantly lower applying scatter correction. The recovery coefficients curve may be subject to an error because of the uncertainty in the reference region of interest resulting from the lack of attenuation correction.

TABLE 3
Comparison of Sensitivity and Spatial Resolution of Selected Small-Animal PET Systems

Category	Quad-HIDAC (14, 15)	microPET II (11)	VISTA (16)	Inveon (10, 12)	NanoPET/CT*
FWHM spatial resolution at CFOV	1.4 (averaged for tangential, radial, and axial)				
Tangential (mm)	1.078	0.83		1.51	1.18
Radial (mm)	1.081	0.86		1.52	1.03
Axial (mm)	1.038	1.25		1.32	0.98
Sensitivity, maximum at CFOV (%)	1.52	2.26	4	9.32	7.7

*FWHM spatial resolution for NanoPET/CT was at one-quarter FOV.

Because NEMA NU 4 standard was published in 2008, only Inveon scanner's data are measured in accordance with this standard. For all other cases, measurements most similar to NEMA NU 4 standard are presented.

Despite the lack of corrections due to the early stage of the instrument and the relatively unsophisticated reconstruction used in this assessment, in the performed image study with ^{18}F -tetrafluoroborate, the 2 lobes of the thyroid were clearly distinguishable, despite the small size of these structures (diameter, ~ 1 mm; length, ~ 2 mm). For further improvement of the image quality, a new, graphical processing unit-based, fully 3D reconstruction, including a detector model and several corrections, has recently been developed by Mediso Ltd. and will shortly be implemented and evaluated.

CONCLUSION

In this article, we evaluated the performance of the NanoPET/CT small-animal PET scanner according to the NEMA NU-4 standard. The main performance parameters are all similar to or exceed those of comparable systems. The spatial resolution approached 1 mm on the axis, which is the highest among currently available commercial systems, and is primarily attributable to the fine 1.17-mm pitch of the detector crystals. The sensitivity and counting rate capabilities have proved adequate for all applications undertaken to date, and the image-quality phantom studies demonstrated good values of uniformity and recovery coefficients even with unimplemented corrections. During the mouse study, the animal-handling facilities provided good accessibility, and small structures, for example, the 2 lobes of the thyroid, are clearly delineated on the images. A new fully-3D reconstruction algorithm taking advantage of the high intrinsic spatial resolution of the scanner is under development.

DISCLOSURE STATEMENT

The costs of publication of this article were defrayed in part by the payment of page charges. Therefore, and solely to indicate this fact, this article is hereby marked "advertisement" in accordance with 18 USC section 1734.

ACKNOWLEDGMENTS

We thank the Mediso team for their support: Tamás Bükki, Dávid Völgyes, Béla Mihalik, Balázs Domokos,

Gergely Németh, Sándor Török, Attila Rácz, Kálmán Nagy, Gábor Jakab, and Lajos Vizhánýó. We also thank Maite Jauregui-Osoro for providing the tracer for the mouse study. This work was supported by Wellcome Trust grant GR084052MA. No other potential conflict of interest relevant to this article was reported.

REFERENCES

- National Electrical Manufacturers Association (NEMA). *Performance Measurements for Small Animal Positron Emission Tomographs (PETs)*. NEMA Standards Publication NU 4-2008. Rosslyn, VA: NEMA; 2008.
- Major P, Hesz G, Szlavec A, Volgyes D, Benyo B, Nemeth G. Local energy scale map for NanoPET/CT system. *IEEE NSS Conf Rec*. 2009;NSS:3177–3180.
- Defrise M, Townsend DW, Bailey D, Geissbuhler A, Michel C, Jones T. A normalization technique for 3D PET data. *Phys Med Biol*. 1991;36:939–952.
- Daube-Witherspoon ME, Muehllehner G. Treatment of axial data in three-dimensional PET. *J Nucl Med*. 1987;28:1717–1724.
- Hounsfield GN. Computerized transverse axial scanning (tomography). 1 Description of system. *Br J Radiol*. 1973;46:1016–1022.
- Hudson HM, Larkin RS. Accelerated image reconstruction using ordered subsets of projection data. *IEEE Trans Med Imaging*. 1994;13:601–609.
- Shepp LA, Vardi Y. Maximum likelihood reconstruction for emission tomography. *IEEE Trans Med Imaging*. 1982;1:113–122.
- Goertzen AL, Suk JY, Thompson CJ. Imaging of weak-source distributions in LSO-based small-animal PET scanners. *J Nucl Med*. 2007;48:1692–1698.
- Jauregui-Osoro M, Sunassee K, Weeks AJ, et al. Synthesis and biological evaluation of [^{18}F]tetrafluoroborate: a PET imaging agent for thyroid disease and reporter gene imaging of the sodium/iodide symporter. *Eur J Nucl Med Mol Imaging*. 2010;37:2108–2116.
- Bao Q, Newport D, Chen M, Stout DB, Chatziioannou AF. Performance evaluation of the Inveon dedicated PET preclinical tomograph based on the NEMA NU-4 standards. *J Nucl Med*. 2009;50:401–408.
- Tai YC, Chatziioannou AF, Yang Y, et al. MicroPET II: design, development and initial performance of an improved microPET scanner for small-animal imaging. *Phys Med Biol*. 2003;48:1519–1537.
- Visser EP, Disselhorst JA, Brom M, et al. Spatial resolution and sensitivity of the Inveon small-animal PET scanner. *J Nucl Med*. 2009;50:139–147.
- Muehllehner G. Effect of resolution improvement on required count density in ECT imaging: a computer simulation. *Phys Med Biol*. 1985;30:163–173.
- Missimer J, Madi Z, Honer M, Keller C, Schubiger A, Ametamey SM. Performance evaluation of the 16-module quad-HIDAC small animal PET camera. *Phys Med Biol*. 2004;49:2069–2081.
- Schäfers KP, Reader AJ, Kriens M, Knoess C, Schober O, Schäfers M. Performance evaluation of the 32-module quadHIDAC small-animal PET scanner. *J Nucl Med*. 2005;46:996–1004.
- Wang Y, Seidel J, Tsui BM, Vaquero JJ, Pomper MG. Performance evaluation of the GE healthcare eXplore VISTA dual-ring small-animal PET scanner. *J Nucl Med*. 2006;47:1891–1900.